Zonal Asymmetries, Teleconnections, and Annular Patterns in a GCM

BENJAMIN A. CASH

Center for Ocean–Land–Atmosphere Studies, Calverton, Maryland

PAUL J. KUSHNER

Department of Physics, University of Toronto, Toronto, Ontario, Canada

GEOFFREY K. VALLIS

Geophysical Fluid Dynamics Laboratory, Princeton University, Princeton, New Jersey

(Manuscript received 2 January 2003, in final form 8 July 2004)

ABSTRACT

The influence of zonally asymmetric boundary conditions on the leading modes of variability in a suite of atmospheric general circulation models is investigated. The set of experiments consists of nine model configurations, with varying degrees and types of zonal asymmetry in their boundary conditions. The structure of the leading EOF varies with the zonal asymmetry of the base state for each model configuration. In particular, a close relationship is found between the structure of the EOF and the model storm tracks. An approximately linear relationship is found to hold between the magnitude of the zonal asymmetry of the leading EOF and of the storm tracks in the models. It is shown that this linear relationship extends to the observations.

One-point correlation maps centered on the regions where the EOFs reach their maximum amplitude show similar structures for all configurations. These structures consist of a north–south dipole, resembling the observed structure of the North Atlantic Oscillation (NAO). They are significantly more zonally localized than the leading EOF, but do resemble one-point correlation maps and sector EOFs calculated for a simulation with zonally symmetric boundary conditions. Thus, the leading EOF for each simulation appears to represent the longitudinal distribution of zonally localized NAO-like patterns. This longitudinal distribution appears to be tied to the distribution of high-frequency eddies, as represented by the storm tracks. A detailed momentum budget for each case confirms that high-frequency eddies play a crucial role in producing the NAO-like patterns. Other dynamical processes also play an important role, but vary with the details of the simulation.

1. Introduction

A common view of atmospheric variability, dating to the work of Walker and Bliss (1932), is that low-frequency variability is dominated by regional patterns, with scales that are greater than synoptic but significantly smaller than the full hemisphere. These patterns were investigated quantitatively in, for example, Wallace and Gutzler (1981), and are commonly referred to as teleconnection patterns. In the intervening years, numerous studies (e.g., Dole and Gordon 1983; Barnston and Livezey 1987; Hurrell 1995, 1996; Feldstein 1998) have considered the dynamical mechanisms that underlie these features, as well as their impacts on temperature, precipitation, and other quantities of interest. One of the most prominent of these teleconnection patterns is the North Atlantic Oscillation (NAO). The NAO consists of a dipole pattern in sea level pressure, among other fields, with centers of action in the Atlantic basin over Iceland and the Azores. The NAO has long been considered a dominant pattern of low-frequency variability (here defined as variability on time scales greater than 10 days) during the Northern Hemisphere (NH) winter and significantly influences temperature and precipitation over much of the North Atlantic. Thus, an understanding of this feature is of substantial interest from the standpoint of both practice and theory.

In recent years, the suggestion has been made that the observed low-frequency variability can be better explained by hemispheric-scale, zonally symmetric, rather than asymmetric, modes of variability (see Baldwin and Dunkerton 1999; Gong and Wang 1999;

Corresponding author address: Dr. Benjamin A. Cash, Center for Ocean–Land–Atmosphere Studies, 4041 Powder Mill Rd., Suite 302, Calverton, MD 20705-3106.
E-mail: bcash@cola.iges.org

Thompson and Wallace 1998, 2000; Limpasuvan and Hartmann 2000). This alternate hypothesis has generated a certain amount of discussion and controversy in the literature. In particular, it has been argued (e.g., Wallace 2000) that the Northern Hemisphere annular mode (NAM; defined here as the leading empirical orthogonal function of the surface pressure) and the NAO are in fact two means of describing the same phenomenon. However, considering the NAO to be a regional manifestation of a hemispheric-scale pattern leads to a rather different view of Northern Hemisphere variability than does considering the NAO to be a leading mode in its own right. Specifically, the NAO paradigm suggests that zonally localized phenomena, such as variations in the Atlantic storm track or interaction with the stationary waves, are the most likely causes of the observed variability. In contrast, the zonally symmetric nature of the NAM naturally lends itself to a zonally symmetric cause, involving, for example, troposphere–stratospheric interactions. Hence, the choice of paradigms exerts a significant influence over the focus of research into the phenomena.

In a companion paper (Cash et al. 2002, hereafter CKV) we examined the annular modes of an idealized, zonally homogeneous (i.e., the statistics of the model are zonally uniform) GCM. In this model, the annular mode approaches, for sufficiently long integrations, a zonally symmetric structure that is in many ways consistent with the observed annular mode. However, this structure is not representative of the underlying low-frequency variability of the model. Rather, we find that the dominant patterns of low-frequency variability are zonally localized dipoles with structures similar to that of the NAO. We suggest that similar conclusions may hold for the observed annular mode.

In the current study, we extend CKV to include a suite of idealized models, with varying degrees and types of zonal asymmetry in the boundary conditions. By comparing results from the zonally homogeneous and inhomogeneous models, we can quantify the impact of lower boundary zonal asymmetries on the leading modes of variability in a simplified setting. In particular, we are interested in understanding how both the leading EOF and the teleconnection patterns evolve as the zonal asymmetry of the model base state increases.

It has been well-established in the literature that temporal and spatial characteristics of the annular modes are controlled by dynamics internal to the atmosphere (e.g., Robinson 1991; Yu and Hartmann 1993; Feldstein and Lee 1996; Limpasuvan and Hartmann 2000). This literature also makes it clear that although stationary wave activity and stratospheric effects play a role in annular mode variability, neither control its tropospheric structure to leading order. For example, Baldwin (2001) shows that the structure of the Southern Hemisphere (SH) and NH annular modes in the zonally averaged surface pressure is practically identical. Since stationary wave activity is much greater in the NH, this result implies that the annular pattern is independent of the stationary eddies and is therefore controlled by transient eddies. In addition, Thompson and Wallace (2000) and Baldwin (2001) show that the surface annular mode signature is the same whether or not data is included from only the "active" stratospheric seasons (when extratropical stratospheric variability is strong and the annular mode extends into the stratosphere) or from all seasons. This implies that the annular mode is, to first order, determined by tropospheric processes. Indeed, the literature suggests an even simpler picture: Robinson (1991) captures basic annular-mode-type variablity with a two-layer model, and Vallis et al. (2004) show using a single-layer model that the annular mode might represent "stirred" barotropic dynamics with the stirring provided by the baroclinic eddies. These findings make it clear that, for our current climate, stratospheric and stationary wave effects on the annular mode structure represent fairly small amplitude perturbations to a basic structure that is controlled by transient baroclinic eddies in the troposphere. This motivates our approach of focusing on stationary wave impacts by introducing zonal asymmetries into the lower boundary in a controlled way.

The paper is organized as follows. In section 2, we describe the base model used for all simulations discussed here, as well as the details of the individual runs that make up the suite of experiments. The base states from three models, chosen to represent the range of asymmetries in the study, are also considered in detail. In section 3, we present the leading EOFs for the same three models, and describe the relationship between the EOFs and the model base states. In section 4, we compare the leading EOFs and the teleconnection patterns. Finally, in section 5 we present a summary and our conclusions.

2. Models and simulation characteristics

a. Model configurations

The simulations examined in this study are based on the same model used for the zonally homogeneous simulations in CKV, to which readers are referred for a more detailed description. Briefly, the model is a spectral AGCM with T42 horizontal resolution and 14 sigma levels vertical resolution, coupled to a 40-m slab mixed layer. The model includes full radiative and moisture packages that are similar to those use previously in the Geophysical Fluid Dynamics Laboratory (GFDL) "R15" and "R30" AGCMs (e.g., Manabe et al. 1979), and is forced by seasonally varying insolation. Each simulation is run for a total of 30 years, with analysis performed on the last 20 years. All analyses presented here were performed for the winter season (December–February in the NH, June–August in the SH). However, as all of the models have identical boundary conditions for the Northern and Southern Hemispheres, winter seasons for the two hemispheres are combined for each run to produce a 40-yr record.

The experiments performed in this study consist of introducing zonal asymmetries of varying strengths and configurations into the boundary conditions of the base model. These asymmetries are introduced in two ways. In one method, the depth of the mixed layer is reduced for half of the domain (see Fig. 1a for configuration). This shallow region is used to simulate land. The depth of the shallow region, relative to the base depth of 40 m, determines the strength of the zonal surface temperature gradient in the presence of seasonally varying insolation, and hence the magnitude of the zonal asymmetry in the simulation base state. Only the depth of the shallow layer is varied from run to run, the horizontal dimensions being fixed. Our other method of introducing asymmetries in the model is the addition of a Gaussian mountain, with a varying maximum height. The horizontal scale is chosen to be roughly equivalent to that of the Tibetan Plateau and is meant to be a simplified representation of this feature (see Figs. 1b,c). Similar to the asymmetries introduced through changing the mixed-layer depth, only the height of the mountain varies between runs. In total, nine model configurations have been analyzed using various combinations of mixed-layer depths and mountain heights (see Table 1 for summary).

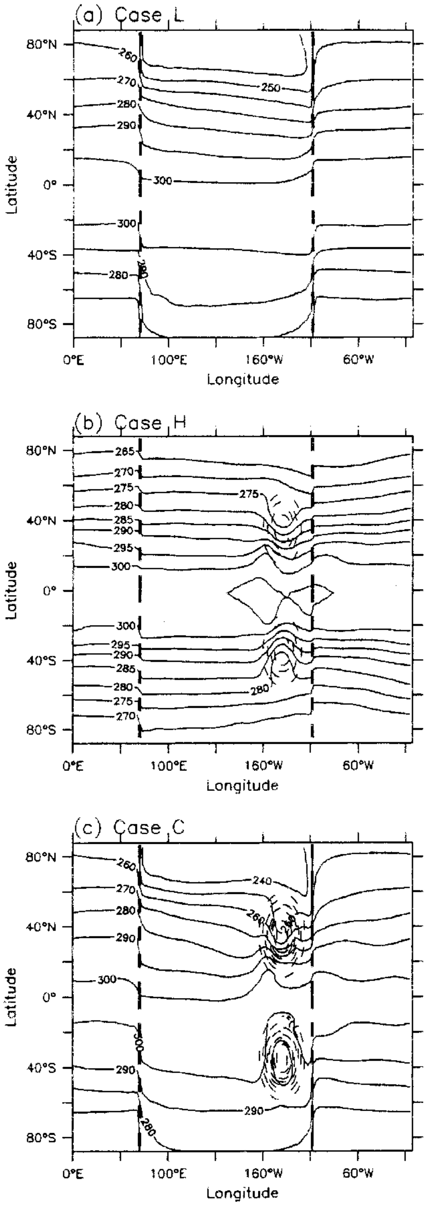

FIG. 1. The NH winter mean surface temperature for (a) L case, (b) H case, and (c) C case. Contours are surface temperature (K), heavy dashed lines denote edge of shallow mixed layer representing land [20 m in (b), 10 cm in (c)], and the dotted contours denote the Gaussian mountain [max height is 2500 m in (b), 5000 m in case (c)].

In this study, we present a detailed analysis of three of these experiments. These three cases, in conjunction with the aquaplanet configuration described in CKV, span the range of boundary asymmetries. In all discussions of the model configurations, "land" refers to a shallow region of the mixed layer (i.e., depths less than 40 m), "mountain" refers to the Gaussian mountain, and "ocean" refers to regions of 40-m mixed-layer depths.

b. Description of model base states

In the first model configuration examined in this study, referred to as L, (see Table 1) the only zonal asymmetry introduced consists of reducing the mixed-layer depth to 10 cm in the land portion of the domain (see Fig. 1a). The resulting zonal gradient in heat capacity produces a strong seasonal cycle in the zonal temperature with a magnitude similar to that seen in the observations (Peixoto and Oort 1992). Zonal tem-

TABLE 1. Experimental design. The table below lists the mountain heights and mixed-layer depths used to simulate land in each of the experiments considered in this study. For all cases, the shallow mixed-layer region representing land extends from 90°S to 90°N, 70°E to 110°W. The Gaussian mountain is centered at 140°W and 35° latitude in each hemisphere. Half-width is 15° in both latitude and longitude. Experiment A refers to an aquaplanet, with a 40-m mixed-layer ocean everywhere and no distinguishable land. Experiment L has a (saturated) landmass of small heat capacity but no mountain. Experiment H has a midsize mountain and a mild contrast between land and ocean. Experiment C has landmass and a mountain and is the most zonally asymmetric of all. The other configurations are combinations of these, and are referred to by number.

	Mountain height		
Land depth	0	2500	5000
10 cm	L	1	C
20 m	2	H	3
40 m	A	4	5

perature contrasts range from 10° to 20°C in the midlatitude to polar regions, in rough agreement with observed Northern Hemisphere winter values.

In the second model configuration considered, referred to as H, we introduce a Gaussian mountain with a maximum height of 2500 m, and a mixed-layer depth of 20 m in the land portion of the domain (Fig. 1b). As we would expect, while the land–sea contrast and the associated zonal asymmetry in the temperature are not negligible, they are considerably weaker for the H case than for the L case.

Finally, we consider the combined impact of land and topography, a configuration referred to as C, by including both land (with a depth of 10 cm) and the Gaussian mountain discussed above, now with a maximum height of 5000 m (Fig. 1c). Note that the mountain is not centered over the land, but is instead at roughly the same displacement from the east coast of the land as Tibet is from the eastern Asian coast.

As we would expect, the different model configurations result in significantly different mean states in all variables, not only surface temperature. In the L case (Fig. 2a), we see that the sea level pressure (SLP) in the NH is dominated by a cold high over land near 30°N and a warm low over the ocean near 60°N. Consistent with observations, we find summer subtropical highs over the oceans. The horizontal extent of these features is clearly controlled by the width of the land and ocean regions.

In the H case, the primary zonal asymmetries in SLP lie downstream of the mountain (Fig. 2b), with relatively low pressure at high latitudes and higher pressures toward the pole. The zonal asymmetries in the land region are reduced relative to the L run, consistent with the reduction in zonal temperature anomaly. The C run shows elements of both the L and H runs (Fig. 2c) with strong zonal asymmetries in both the land and ocean regions of the domain.

The influence of the different boundary conditions is also clearly visible in the upper levels of the model. In the L case, the zonal jet at 200 mb (Fig. 3a) begins near the downstream edge of the land at 35°N latitude. The jet extends effectively the length of the ocean basin and shows little meridional tilt. In contrast, the jet in the H case (Fig. 3b) is closely confined downstream of the mountain and shows a distinct southwest–northeast tilt. The contrast between the Northern and Southern Hemispheres is reduced relative to case L, consistent with the greater thermal inertia of the 20-m mixed-layer depth in the land region. In the C run, the jet is more sharply localized than in either of the other runs, reaching its maximum value just off the downstream edge of the continent. The position and magnitude of the jet relative to the terrain features is in qualitative agreement with the observed position and intensity of the NH wintertime Pacific jet.

The differences between the three model runs are particularly clear in their stationary wave patterns. The L run (Fig. 4a) displays a relatively simple wavenumber-1 pattern in the midlatitudes, with lowered heights over the ocean region. In the H run (Fig. 4b) the most significant feature is a small region of lowered heights to the northeast of the mountain. As with the upper-level jet, the C run (Fig. 4c) displays features related to both the L and H runs.

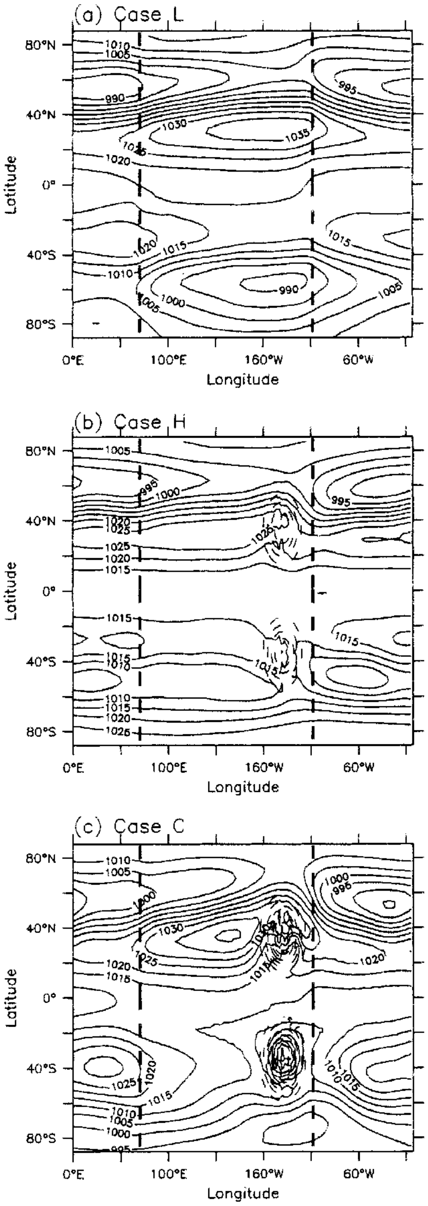

FIG. 2. The NH winter mean sea-level pressure for the (a) L case, (b) H case, and (c) C case. Contours are SLP, heavy dashed lines denote the edge of the shallow mixed layer representing land [20 m in (b), 10 cm in (c)], and dotted contours denote the Gaussian mountain [max height is 2500 m in (b), 5000 m in (c)].

In summary, the three configurations of the model boundary conditions result in zonal asymmetries that are distinct for each run, from the weakly zonally inho-

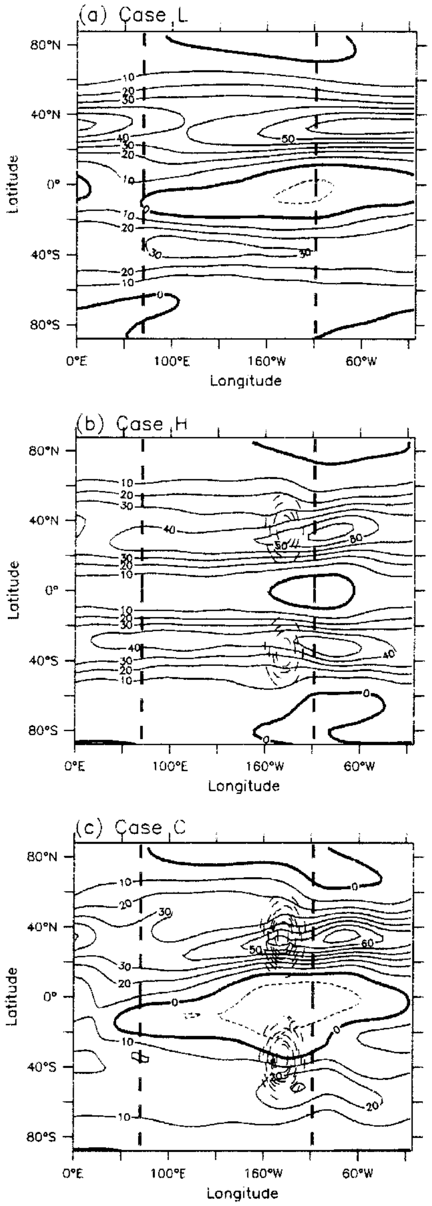

FIG. 3. The NH winter mean 200-mb zonal winds for the (a) L case, (b) H case, and (c) C case. Contours (solid and dashed) are 200-mb zonal wind; heavy dashed lines denote edge of shallow mixed layer representing land [20 m in (b), 10 cm in (c)]; and dotted contours denote the gaussian mountain maximum height 2500 m in (b) and 5000 m in (c).

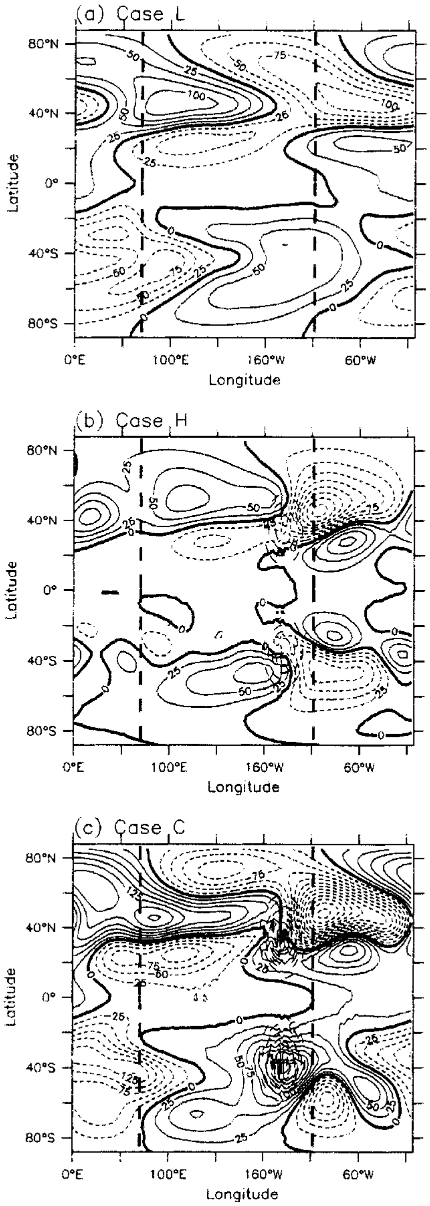

FIG. 4. The NH winter mean 200-mb stationary waves for the (a) L case, (b) H case, and (c) C case. Stationary waves are defined here as deviations of the winter mean 200-mb geopotential heights from their winter mean zonal mean. Contours (solid and dashed) denote geopotential height anomaly. Solid lines are positive, dashed lines are negative. Other features as given in Fig. 3.

mogeneous L run to the fairly realistic C run. This make them suitable for examining the impact of varying asymmetries on the structure of the leading EOFs.

3. Annular modes

As a means of characterizing the low-frequency variability of each model, we calculate the leading EOF of the surface pressure. For this calculation, we first remove the seasonal cycle by subtracting the calendar mean of the surface pressure at each day. The resulting data is then 10-day low-pass filtered and area weighted by the square root of the cosine of the latitude. This filtered, weighted data is then used to calculate the leading EOF for each model (Fig. 5).

In the meridional direction, the structure of the leading EOF is similar for each model over most of the domain. Each EOF consists of a dipole, with maxima in

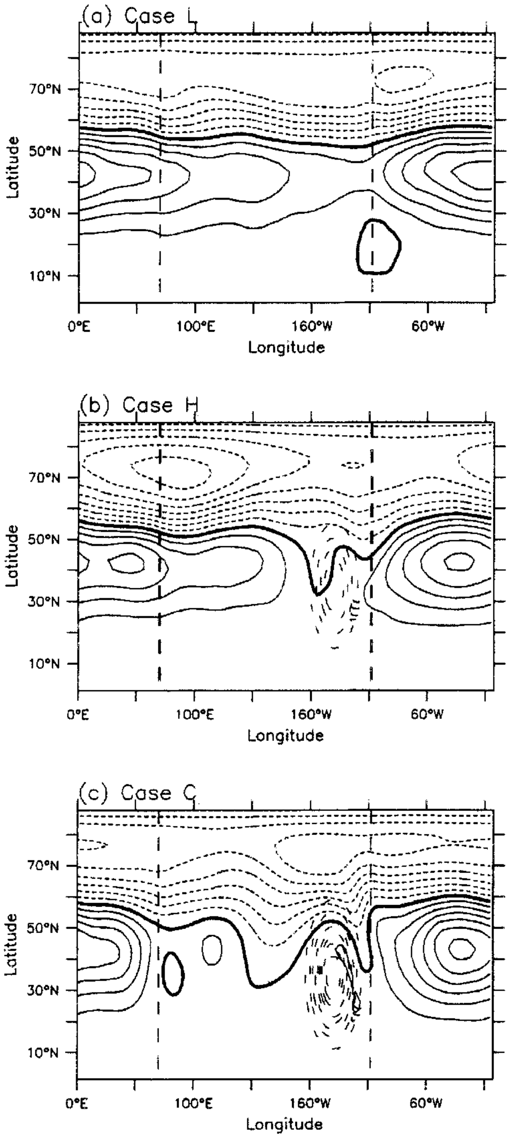

FIG. 5. Annular mode for the (a) L case, (b) H case, (c) and C case. Annular modes are defined as the leading EOF of the surface pressure for each model. Solid contours are positive; dashed lines are negative. Other features as given in Fig. 3.

the polar region and the midlatitudes and the node falling near 60°N latitude. However, the zonal structure of the modes clearly varies with the zonal inhomogeneity of the base state of the model. In the L case, positive loadings extend around the entire hemisphere (Fig. 5a) with the maximum midlatitude values of the EOF downstream of the land region. In the H case (Fig. 5b), the EOF is more localized over the ocean and the EOF maximum is again located downstream of the terrain feature. The C run (Fig. 5c) EOF is even more localized over the ocean and the location of the maximum is similar to the previous runs.

Comparing the structure of the leading EOFs to the model base states, we find that for each model the leading EOF takes on its maximum amplitude in the midlatitudes, slightly downstream of the zonal jet (cf. Figs. 3 and 5). This suggests that processes in the jet exit region may be playing a role in determining the position and amplitude of the leading EOF. To investigate this more directly, we compare the position of the model storm tracks and leading EOFs (Fig. 6). Here we define the storm track as the time-mean 2–10-day band-pass-filtered eddy kinetic energy, vertically averaged from 1000 to 100 mb. The correspondance between the EOFs and the storm tracks is clearly not exact, as demonstrated by Figs. 6a and 6b. One possible explanation for these differences is a lack of robustness in the fine structure of the EOFs. It is also likely that other processes (such as interaction with the stationary waves) are also influencing the location and structure of the EOF, and that the EOF is not determined exclusively by the high-frequency eddies. This is explored in greater detail below. However, in general, the zonal variations in the leading EOF are closely related to the zonal variations in the model storm track.

This relationship is further illustrated by comparing the deviations from zonal symmetry in the leading EOF to the deviations from zonal symmetry in the storm track (Fig. 7) for *all* model configurations listed in Table 1. As is apparent from Fig. 7, the increase in the zonal asymmetry of the EOF is accompanied by an approximately linear increase is the asymmetry of the kinetic energy, at least for smaller EOF asymmetry values. As the asymmetry of the base state increases, the asymmetry of the leading EOF and the storm tracks saturates. These cases correspond to the cases with relatively large land–sea contrast or orographic forcing (cases 1, 3, and C in Table 1).

The relationships exhibited in Fig. 7 extend to the real climate system. Also included in Fig. 7 are points for the Northern Hemisphere and Southern Hemisphere winter seasons, as determined from the National Centers for Environmental Prediction–National Center for Atmospheric Research (NCEP–NCAR) reanalysis data. The SH point falls within the cluster of points associated with relatively little orographic influence (experiments L, H, and 4 from Table 1). The NH data point is more of an outlier but lies closest to the strongly asymmetric experiments. We note that there are important differences in detail between the observed and simulated EOF/storm-track structures. In particular, in the observations, the EOF maxima lie downstream of the storm-track maxima. This is in contrast to the simulations, in which the EOF maxima coincide with or lie upstream of the storm tracks (Fig. 6). In spite of these differences, the conclusion is that there is a strong positive link between the strength of the EOF asymmetries and the strength of the storm-track localization in both the models and the observations.

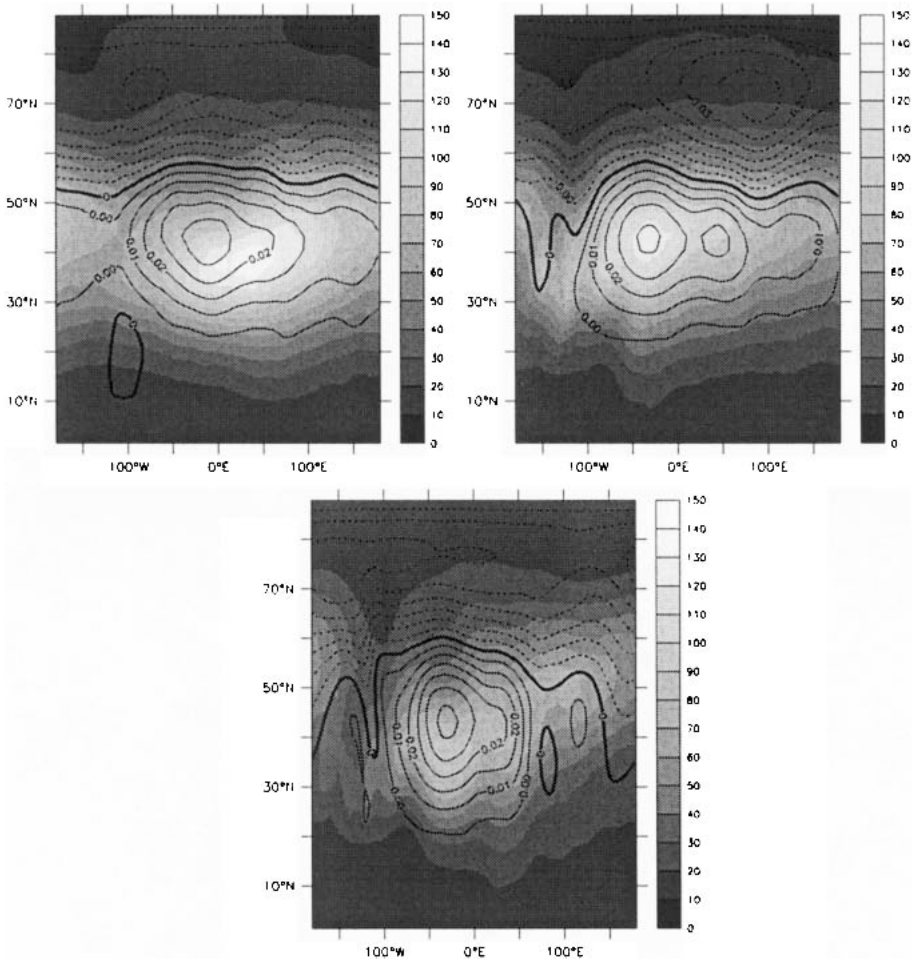

FIG. 6. Comparison of leading EOF and storm track for the (a) L case, (b) H case, and (c) C case. Shading denotes model storm track, as defined by the vertically averaged 2–10 bandpass-filtered eddy kinetic energy. Contours denote the model leading EOF. Solid contours are positive; dashed lines are negative. Geographical features have been omitted for clarity; see Fig. 5 for orientation.

4. Teleconnection patterns

We have seen that there is a relationship between the spatial structure of the EOFs and the localization of the storm tracks, but the physical significance of this relationship needs to be clarified. One issue is that the leading EOF may not be representative of the underlying patterns of variability (CKV; Ambaum et al. 2001). In the observations and in the zonally homogeneous model, one-point correlation maps (also referred to as teleconnection patterns) reveal that the dominant patterns of low-frequency variability are zonally localized, with characteristic zonal scales of approximately 60° longitude. These teleconnection patterns are also similar in structure to the leading EOF of the model, defined for a limited longitudinal sector (CKV), in having a meridionally oriented dipole (see Fig. 8). This indicates that these localized dipoles represent a prevalent pattern of low-frequency variability in the aquaplanet model (A in Table 1) and that the zonally symmetric nature of the leading EOF arises from the homogeneous distribution of these zonally asymmetric features.

To investigate the relationship between the leading EOFs and the underlying data in the zonally inhomogeneous models, we calculate one-point correlation maps for each point in the model domain. The strength of the teleconnection pattern for each base point is defined as the absolute value of maximum anticorrelation that is found, anywhere in the domain, for that base point. Examining the geographical distribution of teleconnection strength (Fig. 9), the base points with the strongest teleconnections are usually found near the centers of action of the leading EOF. We also find that the weakest teleconnections tend to occur along the nodal lines of the EOFs. In the L and H configurations, of the model (Fig. 9), we see that the strongest teleconnections are generally collocated with the maxima of

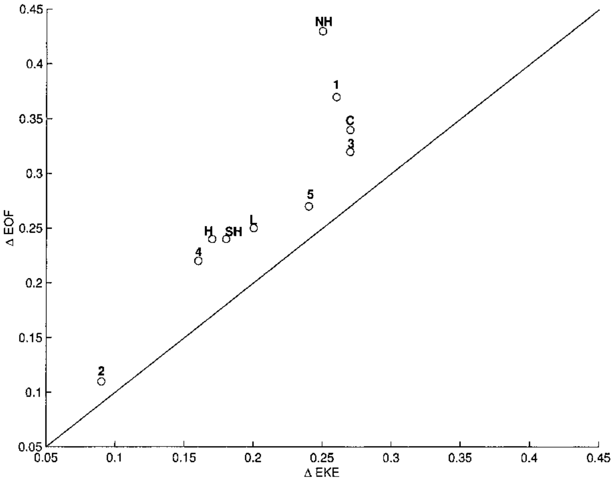

FIG. 7. Comparison of zonal asymmetry of leading EOF with zonal asymmetry of the storm track. Zonal asymmetry is defined as rms deviation from zonal mean for both quantities, normalized by zonal mean values. All values are averaged meridionally from equator to pole. In addition, eddy kinetic energy is vertically averaged from 1000 to 100 mb. Labels as given in Table 1, and NH and SH refer to Northern and Southern Hemisphere winters, respectively.

the leading EOF. In the C configuration, there are two distinct regions with strong teleconnections. One region, lying near the position of the mountain (160°W longitude) is not particularly similar to the EOF and may be due to the presence of the mountain itself. The second region of strong teleconnections does resemble a zonally localized version of the EOF, which suggests that the two features are related.

The correspondence between the strongest teleconnections and the centers of action of the EOFs also holds in the other model integrations we have performed (not shown). In the zonally homogeneous model in CKV, we found, similarly, that the meridional locations of the EOF centers of action corresponded to the meridional location of the strongest teleconnections. Figure 9 shows that this relationship extends to the zonally inhomogeneous case, point by point.

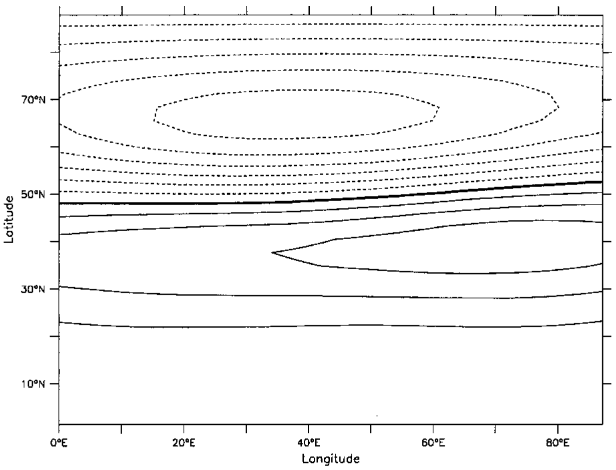

FIG. 8. Sector EOF from zonally homogeneous aquaplanet model (experiment A in Table 1). The EOF is calculated for a domain of 90° longitude from the aquaplanet model used in CKV. (Reproduced from CKV, Fig. 11a.)

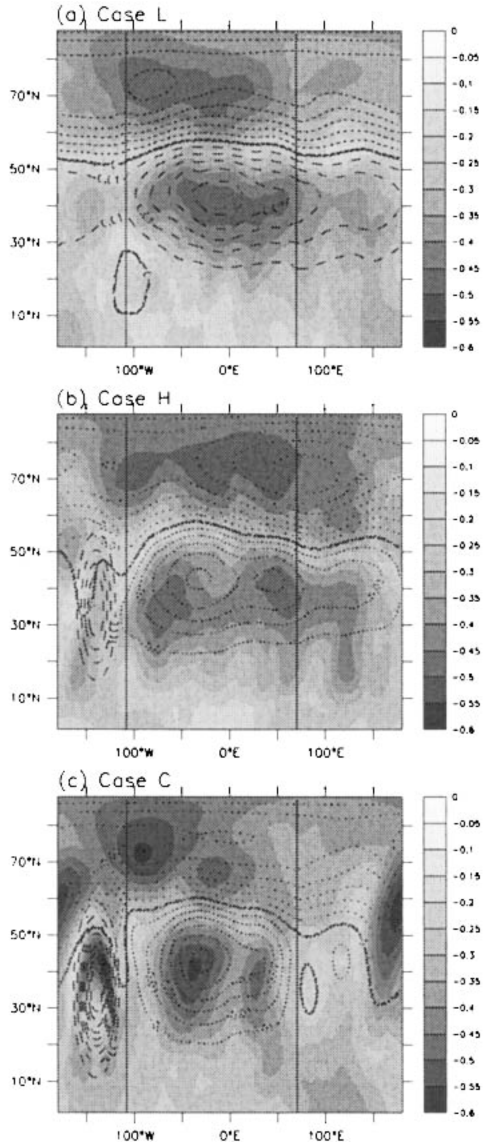

FIG. 9. Comparison of maximum anticorrelation and leading EOF for the (a) L case, (b) H case, and (c) C case. At each point the shading denotes the value of the maximum anticorrelation attained for that basepoint, and contours denote the model leading EOF. Solid contours are positive, dashed lines are negative.

Having established that a similar relationship exists between the teleconnections in the zonally homogeneous and inhomogeneous models, we now consider the structure of those teleconnections. Similar to the analysis of Wallace and Gutzler (1981), we examine the one-point correlation map for the base point with the maximum anticorrelation for each of the three simulations considered here (Figs. 10a–c). Although there are some variations between individual models, the general pattern is clearly that of a dipole, with the low-latitude center falling near 40° latitude and a higher-latitude center near 80°. Of particular interest is the similarity of the teleconnection patterns derived for the zonally inhomogeneous models to that calculated for the CKV aquaplanet model (A in Table 1, cf. Fig. 10d). The centers of the teleconnections are also offset in the east–west direction by about 20° longitude in each configuration, similar to the sector EOF.

The similarity between the teleconnections and the sector EOF from the A case shown in Fig. 8, combined with the overlap between the regions of strong teleconnections and the leading EOFs, suggests that the annular mode represents the averaged longitudinal distribution of individual events that have a structure similar to that of the teleconnections. To test this hypothesis, we calculate a measure of the average pattern correlation (defined as the geographical correlation between two maps) between the sector EOF (Fig. 8) and the low-pass filtered surface pressure as a function of longitude for each of the model configurations. The methodology of this test is as follows. For each configuration, we first center the sector EOF at a given longitude. We then calculate the time-mean of the absolute value of the pattern correlation between the sector EOF and the low-pass filtered surface pressure in the sector of the model corresponding to the location and dimensions of the EOF. The resulting pattern correlation magnitude is recorded for the chosen central longitude, and the process is then repeated for each longitude in turn.

For each run, the resulting correlation plots show good agreement with the structure of the respective EOFs (Fig. 11). Correlations reach their peak values downstream of the terrain features and, in general, follow the amplitude of the low-latitude center of the EOF. This supports the hypothesis that individual events have structures similar to the sector EOF, and

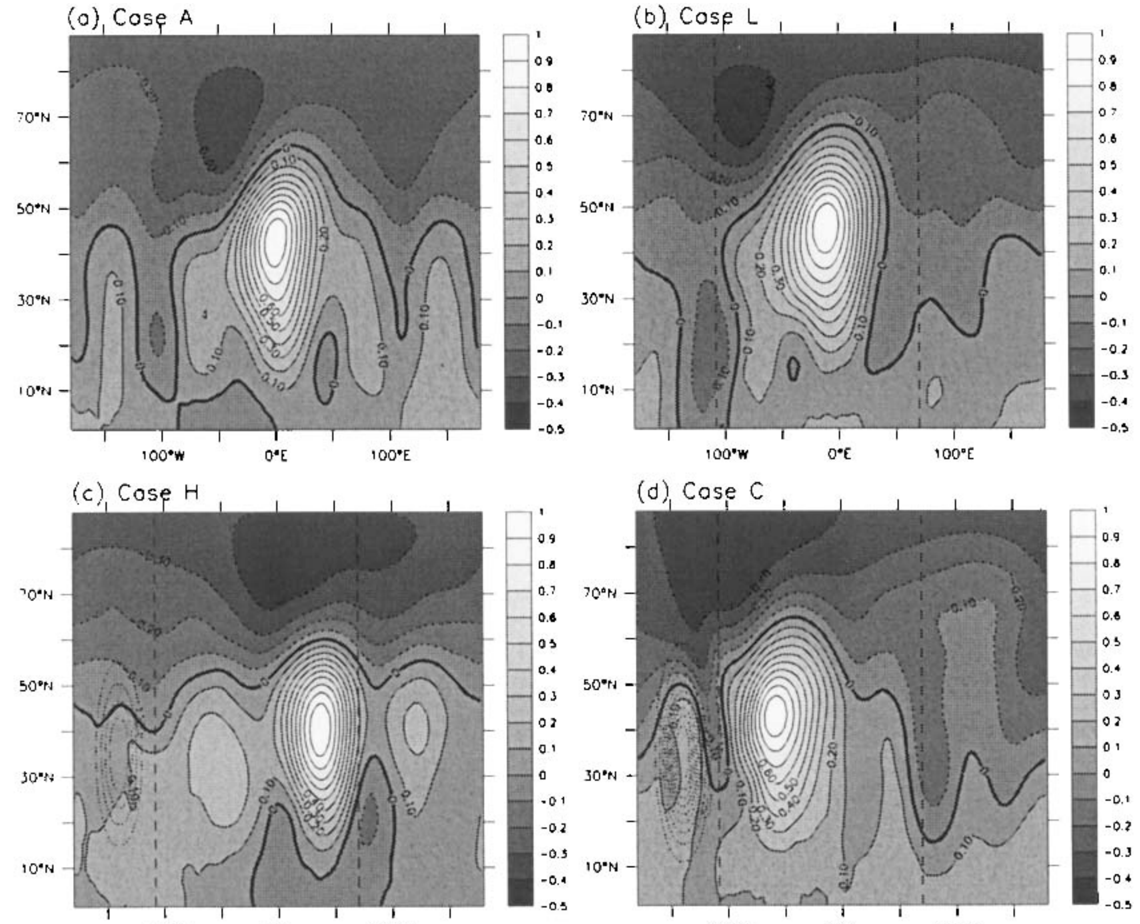

FIG. 10. Teleconnection patterns for the (a) A case (from CKV), (b) L case, (c) H case, and (d) C case. Contours denote one point correlation maps, taken for the base point of the maximum anticorrelation for each model. Solid contours are positive, dashed lines are negative, and the contour interval is 0.1. Shading also denotes correlation. Note ocean region is in the center of each panel.

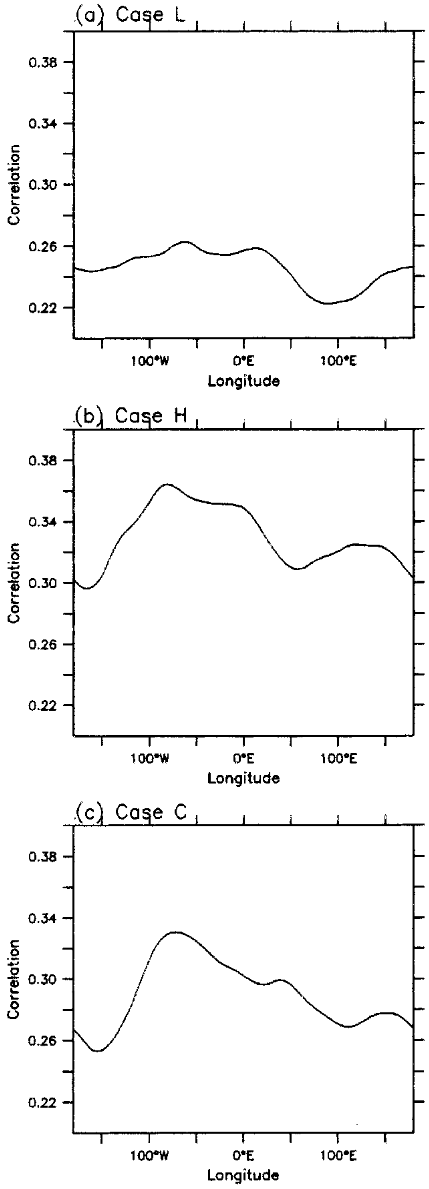

FIG. 11. Pattern correlation between low-pass-filtered surface pressure from the (a) L case, (b) H case, and (c) C case and sector EOF. Values represent pattern correlation with sector EOF shown in Fig. 8, centered at the given longitude. The value for the aquaplanet model is 0.38.

that the hemispheric EOF represents the distribution of these events. In general, it appears that the leading EOF for each model can be thought of as reflecting the distribution of the dipole patterns. The fact that the agreement is in general fairly close is remarkable, given that the sector EOF is derived from a separate model, and is a testament to the robustness of the localized dipole. If this analysis is applied to the aquaplanet model, from which the sector EOF is derived, we find an average value of 0.38. The magnitudes for cases H and C are very close to this value in the regions where the EOF has a large magnitude, suggesting dynamical features similar to those seen in the aquaplanet model dominate in these regions. The values for case L fall significantly below the aquaplanet value, for reasons that are not immediately clear.

Given the similarity between the model teleconnections and the NAO, and the fact that regions of high teleconnection strength tend to correspond to high amplitudes of the leading EOF, a number of features of the model can now be explained. Numerous studies have linked the existence and behavior of the NAO to the storm tracks (e.g., Rogers 1990; Hurrell 1995; Gulev 1997; DeWeaver and Nigam 2000). While the relationship between the storm tracks and the NAO is complex, and not fully understood, evidently the high-frequency transients play an important role in governing the NAO.

Similar to the observations, the most prominent teleconnections in our models occur near the storm tracks. Thus, it appears that the relationship between the leading EOFs and the storm tracks in our models comes about through the link between the high-frequency transients and the NAO-like teleconnection patterns. Consistent with the leading EOFs/annular modes of the zonally homogenous model in CKV, the leading EOFs/annular modes of the zonally inhomogeneous models represent the longitudinal distribution of the dominant teleconnection patterns, rather than representing a single, dynamical feature. Unlike CKV, the teleconnection patterns are now distributed inhomogeneously in longitude. The characteristics of that distribution appear to be governed by the storm tracks.

To further investigate the relationship between the teleconnections and the high-frequency transients, we define a teleconnection index for each model configuration. Similar to the NAO index used by Wallace and Gutzler (1981), we define the teleconection index for a given model configuration as the difference between the surface pressure at the high-latitude and low-latitude centers of the telconnection pattern. Thus, to take the C model configuration as an example, the index is defined as

$$I(t) = P_s(75°\text{N}, 100°\text{W}) - P_s(45°\text{N}, 10°\text{W}), \qquad (1)$$

where P_s is the surface pressure.

We now assess, in a simple way, the role of the high-frequency transient eddy forcing in the teleconnection events. To do so, we lag-regress the zonal wind anomaly (Fig. 12, contours) and the momentum flux convergence from the high-frequency eddies (Fig. 12, shading) against the teleconnection index (normalized by its standard deviation) for each case. The regressed zonal wind anomaly and eddy forcing are zonally averaged over a 90° longitude region centered on the teleconnection, and vertically averaged from 500 to 100 mb. In both the zonally inhomogeneous (Figs. 12a–c) and the zonally homogeneous (Fig. 12d) configurations, we see a dipole pattern in the zonal wind anomalies asso-

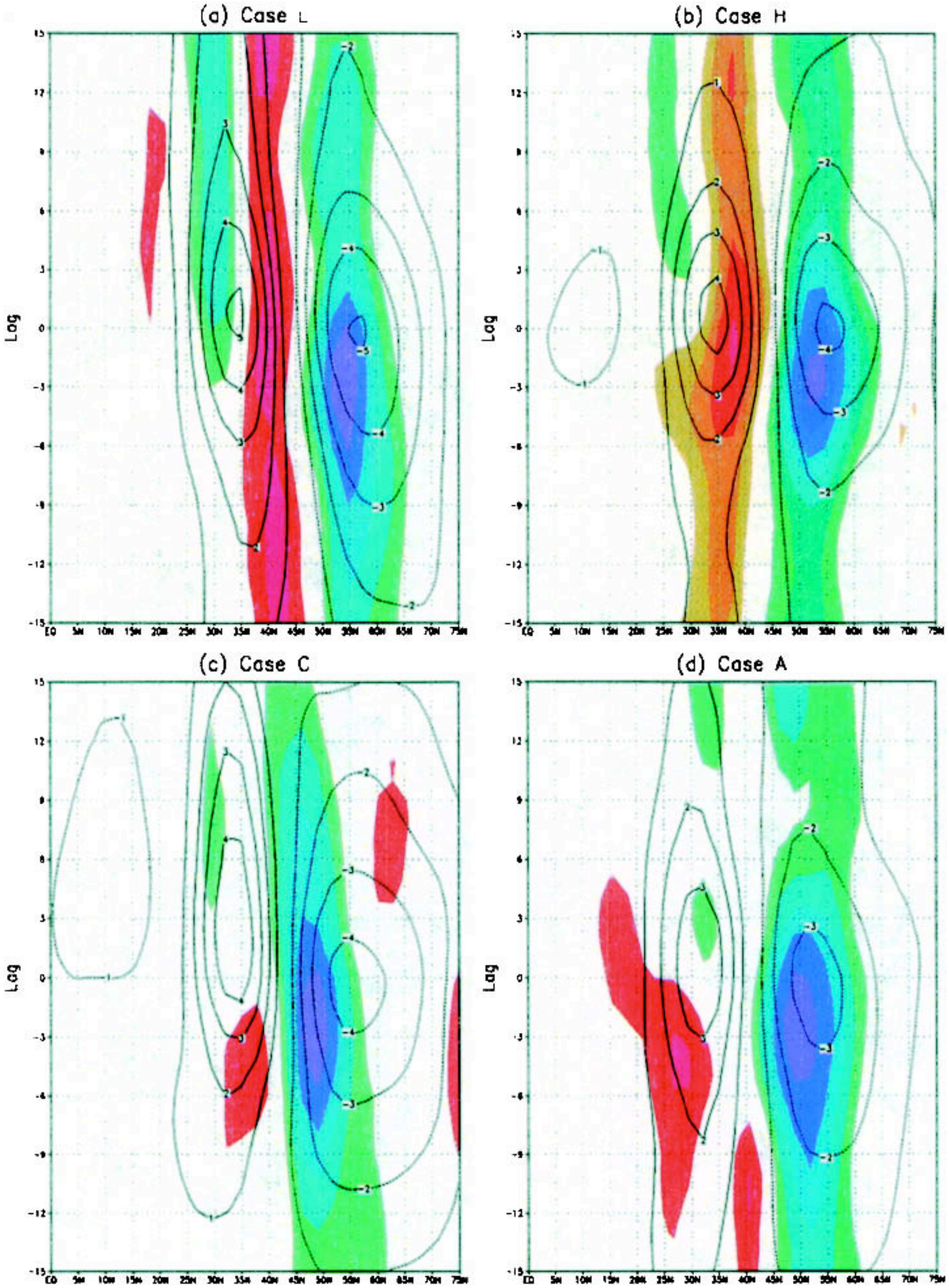

FIG. 12. Regressed zonally and vertically averaged zonal wind anomalies (contours) and anomalous eddy momentum flux convergence (shading) for the (a) L case, (b) H case, (c) C case, and (d) A case (from CKV). Units of wind are in m s^{-1}; momentum flux covergence are in m s^{-1} day^{-1}; values are for 1 std dev of the teleconnection index. Shading interval is 0.1 m s^{-1} day^{-1}.

ciated with a shift in the maximum of the zonal jet. Similarly, we find a dipole pattern of the same sign in the eddy forcing, which tends to lead the dipole in the zonal winds on the order of a few days. It is particularly noteworthy that the results for the zonally homogeneous and inhomogeneous models are quite similar, strengthening the view that the dynamical processes governing the dominant patterns of low-frequency variability are similar in each case, and only the preferred location of occurence changes between models. It is important to note, however, that the high-frequency eddies are not solely responsible for the existence of the dipole in the zonal wind. Depending on the integration, other dynamical processes also contribute, particularly to the formation of the positive wind anomaly. For case A, both low-frequency nonlinear interactions and interactions between the eddies and the zonal mean flow also play a role. For case C, interactions with both the zonally symmetric and asymmetric components of the mean flow contribute to the positive wind anomaly. The influence of these dynamical processes helps to explain why the linkage between the storm track and the leading EOF is not exact in each model. However, nonlinear interaction between the high-frequency eddies is the only dynamical process that contributes strongly to the zonal wind anomaly in each integration.

5. Summary and conclusions

In this study, we have considered the leading patterns of variability in a suite of idealized GCMs. For each model configuration, different asymmetries were introduced in the boundary conditions, and the impact of these asymmetries on the model annular modes was investigated. We find that a robust relationship exists between the zonal inhomogeneity of the model base state and the zonal asymmetry of the leading EOF. In particular, the leading EOF of the surface pressure tends to follow the structure of the model storm track, as defined by the vertically averaged bandpass-filtered eddy kinetic energy. As the zonal asymmetry of the model base state increases, the storm tracks and leading EOFs become increasingly zonally localized. Consistently, the regions in which we find strong teleconnection patterns also become more zonally localized. We find a roughly linear relationship between the zonal asymmetry of the EOF and of the storm tracks, a relationship that extends to the observations. Of course, one must be cautious in making any direct comparisons between our model and observations because of the highly idealized nature of the simulations performed. However, as NAO-like patterns are found across a wide range of model complexities, it seems reasonable to assume that the GCM representation of these features can at least provide insight into their behavior in the atmosphere.

As in CKV and Ambaum et al. (2001), we find that the leading EOF does not resemble the zonal covariance structure of the variability. One-point correlation maps consistently demonstrate that the model low-frequency variability (i.e., on the weekly to monthly time scale) tends to be dominated by more localized patterns, with characteristic zonal scales of approximately 60° longitude. Of particular interest is the fact that the scale and structure of the teleconnection patterns are similar between model runs, despite the significant differences in boundary conditions. These differences in boundary conditions appear to manifest themselves primarily in the longitudinal distribution of occurrence of the teleconnections, rather than in the structure of the patterns themselves. We also find that the regions of strongest teleconnections generally follow the pattern of the leading EOF, although the match is not exact in all cases.

The above results lead to the conclusion that the leading EOF of each model generally represents the longitudinal distribution of meridional dipole patterns within the model domain. These patterns resemble the observed NAO, and there is evidence to suggest that this relationship holds in the atmosphere as well. During the NH hemisphere winter, the Atlantic storm track is substantially stronger than the Pacific storm track. This is due, at least in part, to the so-called "midwinter suppression" phenomenon (Nakamura 1992). As is well known, the dipole pattern of the NAO is the dominant pattern of low-frequency variability in the North Atlantic during the winter months. In the North Pacific a lesser known, but still prominent, dipole teleconnection pattern [the North Pacific Oscillation (NPO)] is also observed during the winter (Wallace and Gutzler 1981). Due to the more complex geometry of the NH, patterns such as the Pacific–North American teleconnection pattern are prominent in the observations, but absent from the models considered here. However, the presence of the NAO and the NPO, combined with their relative strength and that of the storm tracks in the respective ocean basins, suggests that the dipole patterns observed in the models represent a physical manifestation of low-frequency variability. For more zonally symmetric geometry, the storm tracks are correspondingly more zonally symmetric and this leads to a more zonally symmetric first EOF, an annular mode. In this picture, the mechanisms producing the NAO and the annular mode are the same, namely, the forcing by baroclinic instability in storm tracks. The dynamics of this has been explored by Vallis et al. (2004). However, forcing by high-frequency eddies may not be the only dynamical process playing a role in creating the NAO-like patterns. Work by DeWeaver and Nigam (2000), among others, indicate that zonal–eddy interactions and stationary waves may play a significant role in maintaining NAO-like anomalies. Consistent with these studies, we do find that other processes, such as zonal–eddy interactions, are important in some of the integrations. We find that the meridional dipolar structure of the pressure field, which is in turn related to the variations in the zonal wind, is the robust physically meaningful structure and that is the building block of both the NAO and the leading EOF.

Acknowledgments. We are grateful for comments from two anonymous reviewers. BAC was supported by the Princeton AOS program and the U.S. Department of Energy (DE-FG02-01ER63256). GKV acknowledges the support of the NSF.

REFERENCES

Ambaum, M. H. P., B. J. Hoskins, and D. B. Stephenson, 2001: Arctic Oscillation or North Atlantic Oscillation? *J. Climate,* **14,** 3495–3507.

Baldwin, M. P., 2001: Annular modes in global daily surface pressure. *Geophys. Res. Lett.,* **28,** 4115–4118.

——, and T. J. Dunkerton, 1999: Propagation of the arctic oscillation from the stratosphere to the troposphere. *J. Geophys. Res.,* **104,** 30 937–30 946.

Barnston, A. G., and R. E. Livezey, 1987: Classification, seasonality, and persistence of low-frequency atmospheric circulation patterns. *Mon. Wea. Rev.,* **115,** 1083–1126.

Cash, B. A., P. J. Kushner, and G. K. Vallis, 2002: The structure and composition of the annular modes in an aquaplanet general circulation model. *J. Atmos. Sci.,* **59,** 3399–3414.

DeWeaver, E., and S. Nigam, 2000: Zonal-eddy dynamics of the North Atlantic Oscillation. *J. Climate,* **13,** 3893–3914.

Dole, R. M., and N. D. Gordon, 1983: Persistent anomalies of the extratropical Northern Hemisphere wintertime circulation: Geographical distribution and regional persistence characteristics. *Mon. Wea. Rev.,* **111,** 1567–1586.

Feldstein, S. B., 1998: The growth and decay of low-frequency anomalies in a GCM. *J. Atmos. Sci.,* **55,** 415–428.

——, and S. Lee, 1996: Mechanisms of zonal index variability in an aquaplanet GCM. *J. Atmos. Sci.,* **53,** 3541–3556.

Gong, D., and S. Wang, 1999: Definition of Antarctic Oscillation index. *Geophys. Res. Lett.,* **26,** 459–462.

Gulev, S. K., 1997: Climate variability of the intensity of synoptic processes in the North Atlantic midlatitudes. *J. Climate,* **10,** 574–592.

Hurrell, J. W., 1995: Decadal trends in the North Atlantic Oscillation: Regional temperatures and precipitation. *Science,* **269,** 676–679.

——, 1996: Influence of variations in extratropical wintertime teleconnections on Northern Hemisphere temperature. *Geophys. Res. Lett.,* **23,** 665–668.

Limpasuvan, V., and D. L. Hartmann, 2000: Wave-maintained annular modes of climate variability. *J. Climate,* **13,** 4414–4429.

Manabe, S., D. G. Hahn, and J. L. Holloway, 1979: Climate simulation with GFDL spectral models of the atmosphere. GARP Publ. Serv. No. 22, WMO, 13 pp.

Nakamura, H., 1992: Midwinter suppression of baroclinic wave activity in the Pacific. *J. Atmos. Sci.,* **49,** 1629–1642.

Peixoto, J. P., and A. H. Oort, 1992: *Physics of Climate.* American Institute of Physics, 520 pp.

Robinson, W. A., 1991: The dynamics of the zonal index in a simple model of the atmosphere. *Tellus,* **43A,** 295–305.

Rogers, J. C., 1990: Patterns of low-frequency monthly sea level pressure variability (1899–1986) and associated wave cyclone frequencies. *J. Climate,* **3,** 1364–1379.

Thompson, D. W. J., and J. M. Wallace, 1998: The Arctic Oscillation signature in the wintertime geopotential height and temperature fields. *Geophys. Res. Lett.,* **25,** 1297–1300.

——, and ——, 2000: Annular modes in the extratropical circulation. Part I: Month-to-month variability. *J. Climate,* **13,** 1000–1016.

Vallis, G. K., E. Gerber, P. J. Kushner, and B. A. Cash, 2004: A mechanism and simple dynamical model of the North Atlantic Oscillation and annular modes. *J. Atmos. Sci.,* **61,** 264–280.

Walker, G. T., and E. W. Bliss, 1932: World weather v. *Mem. Roy. Meteor. Soc.,* **4,** 53–83.

Wallace, J. M., 2000: North Atlantic Oscillation/Annular mode: Two paradigms—One phenomena. *Quart. J. Roy. Meteor. Soc.,* **126,** 791–805.

——, and D. S. Gutzler, 1981: Teleconnections in the geopotential height field during the Northern Hemisphere winter. *Mon. Wea. Rev.,* **109,** 784–812.

Yu, J.-Y., and D. L. Hartmann, 1993: Zonal flow vacillation and eddy forcing in a simple GCM of the atmosphere. *J. Atmos. Sci.,* **50,** 3244–3259.